

# Morphology and CO Oxidation Activity of Pd Nanoparticles on SrTiO<sub>3</sub> Nanopolyhedra

Bor-Rong Chen,<sup>†</sup> Lawrence A. Crosby,<sup>†,‡</sup> Cassandra George,<sup>‡</sup> Robert M. Kennedy,<sup>‡,§</sup> Neil M. Schweitzer,<sup>§</sup> Jianguo Wen,<sup>||</sup> Richard P. Van Duyne,<sup>‡,⊥</sup> Peter C. Stair,<sup>‡,⊥</sup> Kenneth R. Poeppelmeier,<sup>†,‡,⊥,||</sup> Laurence D. Marks,<sup>†</sup> and Michael J. Bedzyk<sup>\*,†,‡,||,⊥,¶</sup>

<sup>†</sup>Department of Materials Science and Engineering, Northwestern University, Evanston, Illinois 60208, United States

<sup>‡</sup>Department of Chemistry, Northwestern University, Evanston, Illinois 60208, United States

<sup>§</sup>Department of Chemical and Biological Engineering, Northwestern University, Evanston, Illinois 60208, United States

<sup>||</sup>Center for Nanoscale Materials, Argonne National Laboratory, Lemont, Illinois 60439, United States

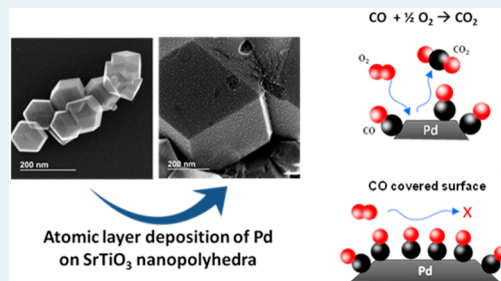
<sup>⊥</sup>Chemical Sciences & Engineering Division, Argonne National Laboratory, Lemont, Illinois 60439, United States

<sup>¶</sup>Department of Physics and Astronomy, Northwestern University, Evanston, Illinois 60208, United States

## S Supporting Information

**ABSTRACT:** Single crystal SrTiO<sub>3</sub> nanocuboids having primarily TiO<sub>2</sub>-(001) surfaces and nanododecahedra having primarily (110) surfaces were created by two separate hydrothermal synthesis processes. Pd nanoparticles grown on the two sets of STO nanopolyhedra by atomic layer deposition show different morphologies and CO oxidation performance. Transmission electron microscopy and small-angle X-ray scattering show that 2–3 nm Pd nanoparticles with 3–5 nm interparticle distances decorate the STO surfaces. When the number of ALD cycles increases, the growth of the Pd nanoparticles is more significant in size on TiO<sub>2</sub>-(001)-STO surfaces, while that on (110)-STO surfaces is more predominant in number. High resolution electron microscopy images show that single crystal and multiply twinned Pd nanoparticles coexist on both types of the STO nanopolyhedra and exhibit different degrees of adhesion. The CO oxidation reaction, which was employed to determine the dependence of catalytic activity, showed that the Pd catalytic performance was dominated by the coverage of CO, which is more directly related to Pd nanoparticle size than to shape. CO turnover frequency analysis and diffuse reflectance infrared Fourier transform spectroscopy show that regardless of the shape or degrees of wetting, larger Pd nanoparticles (~3 nm) have lower catalytic activity due to high CO coverage on nanoparticle facets. Smaller nanoparticles (~2 nm) have more edge and corner sites and exhibit 2–3 times higher TOF at 80 and 100 °C.

**KEYWORDS:** heterogeneous catalysts, palladium, CO oxidation, strontium titanate, atomic layer deposition, X-ray small angle scattering, X-ray absorption near edge structure, diffuse reflectance infrared Fourier transform spectroscopy



## 1. INTRODUCTION

For oxide-supported metallic nanoparticle (NP) catalysts, “metal-support interactions” described by morphological and electronic changes of the NP and the interface can have a major influence on the catalytic activity. The effects include the encapsulation of metal NPs by migration of the support atoms,<sup>1,2</sup> redistribution of interfacial charges,<sup>3,4</sup> participation of surface lattice oxygen in reactions,<sup>5–7</sup> and stabilization of noninteracting metal NPs.<sup>8,9</sup> To reduce the complexity of poorly defined metal/oxide interfaces typical in industrially relevant powder catalysts and to address the support effects, well-defined single crystal oxide substrate surfaces are typically needed.<sup>10–16</sup> However, the relatively low surface area of a single crystal substrate limits the ability to measure chemical kinetics and thereby leads to the so-called “materials gap.”<sup>17–21</sup>

Our strategy for bridging this gap is to employ oxide “nanopolyhedra supports” with well-defined single crystal

facets. The metal/oxide nanopolyhedra system employed in this paper is inspired by earlier work on Pt<sup>22–30</sup> and Pd<sup>31–34</sup> NPs grown on SrTiO<sub>3</sub> (STO) single crystal substrates. Hydrothermal synthesis methods for the STO single crystal nanocuboids with controllable surface terminations have been reported elsewhere<sup>35–38</sup> and recently extended to yield (110)-terminated nanododecahedra.<sup>39</sup> Previously, we studied Pt<sup>8,9,40,41</sup> and Pd<sup>42</sup> NPs grown on STO single crystal nanocuboids with predominantly (001) surfaces and controllable TiO<sub>2</sub> or SrO surface terminations. This advance in synthesis allows direct comparisons of morphology and activity between metal NPs grown on atomically flat and distinct STO nanopolyhedra surface orientations.<sup>39,43</sup> This approach opens

Received: December 5, 2017

Revised: April 9, 2018

Published: April 16, 2018

up opportunities to investigate structural features of the metal/oxide interface at the atomic level, while the high surface-to-volume ratios of the nanopolyhedra supports enable practical catalytic reaction studies.<sup>8,40,41,44</sup>

In this work, we study structure-catalytic activity relationships of atomic layer deposition (ALD)-grown Pd NPs on two types of STO nanopolyhedra: TiO<sub>2</sub>-(001)-terminated nanocuboids and (110)-terminated nanododecahedra. In both cases, the Pd NP size and coverage were controlled by the number of ALD cycles, as demonstrated in our previous studies on Pt and Pd.<sup>26,28,40–42</sup> CO oxidation is employed as a probe reaction to determine and compare the catalytic performance of Pd on the two types of STO nanopolyhedra. This experimental design allows analysis of the effects of NP size, shape, and crystalline termination of the support facets on catalytic performance. The shapes and orientations of the Pt or Pd NPs predicted by thermodynamics using the Winterbottom construction<sup>45</sup> can be affected by the STO chemical termination,<sup>23,42</sup> crystalline orientation,<sup>24,25</sup> and surface reconstruction.<sup>32,33</sup> Furthermore, the catalytic activity of the free-standing Pt or Pd NPs depends upon the exposed crystal facets, as studies have shown that (111) facets of Pt or Pd are significantly more active than (001) facets toward CO oxidation.<sup>46,47</sup> By combining shape-selectable Pd/STO nanopolyhedra catalysts with the structure sensitive CO oxidation reaction, our present study aims to establish the relationship between the Pd NP/STO support interface morphology and catalytic activity. However, our results also show that the catalytic performance of CO oxidation for this system is dominated by CO coverage on the Pd surface, which is more directly related to Pd nanoparticle size than to shape. In addition, the majority of the Pd NPs are multiply twinned particles (e.g., refs 48–53), creating an interesting complexity to the Pd/STO interfacial orientation and adhesion behavior.

## 2. EXPERIMENTAL METHODS

### 2.1. Sample Preparation. 2.1.1. SrTiO<sub>3</sub> Nanopolyhedra.

TiO<sub>2</sub>-(001)-STO nanocuboids and (110)-STO nanododecahedra supports were produced by two separate, previously reported, hydrothermal synthesis methods.<sup>35,39</sup> The two types of supports are single crystal nanopolyhedra with atomically flat facets and negligible edge/corner areas. TiO<sub>2</sub>-(001)-STO nanocuboids have an average edge length of 50–70 nm, while the (110)-STO nanododecahedra have diameters ranging from 100–1000 nm. The specific surface areas of the two types of supports were measured by a standard Brunauer–Emmett–Teller (BET) analysis. TiO<sub>2</sub>-(001)-STO nanocuboids and (110)-STO nanododecahedra showed BET surface areas of approximately 20 and 4 m<sup>2</sup>/g, respectively.

**2.1.2. Atomic Layer Deposition.** Pd was deposited on the two types of STO supports by atomic layer deposition (ALD) at 200 °C using Pd(II) hexafluoroacetylacetonate (Pd(hfac)<sub>2</sub>) and formalin (HCHO) as the precursors. The deposition conditions and experimental setup followed our previous ALD work.<sup>42</sup> In the present work, 1, 5, and 10 ALD cycles of Pd (denoted as 1c, 5c, and 10c) were deposited on both the TiO<sub>2</sub>-(001) and (110) terminated STO nanopolyhedra. The as-deposited ALD-Pd/STO samples were stored in the air before subsequent measurements or catalysis reactions.

**2.2. Characterization Methods. 2.2.1. Electron Microscopy.** The morphological evolution of the Pd/TiO<sub>2</sub>-(001)-STO nanocuboids and Pd/(110)-STO nanododecahedra was measured by a JEOL JEM-2100FasTEM and by a Hitachi H-2300 STEM equipped with a secondary electron (SE) detector. The

high-resolution electron microscopy (HREM) images of Pd nanoparticles were obtained using three instruments: a JEOL JEM-2100FasTEM system at Northwestern University (NU), an aberration-corrected JEOL JEM-ARM200CF at the Research Resources Center at the University of Illinois, Chicago (UIC), and the aberration-corrected ACAT microscope at Argonne National Laboratory (ANL). The size distributions of statistically significant samples of Pd nanoparticles were extracted by using the ImageJ software.<sup>54</sup> The samples measured with electron microscopy, as well as other characterization methods described in the following sections, were as-deposited samples, unless otherwise stated.

**2.2.2. Small-Angle X-ray Scattering (SAXS).** Small-angle X-ray scattering (SAXS) measurements were applied as a complementary technique to the TEM measurements. X-ray scattering data were simultaneously collected by the small-angle and medium-angle Rayonix area detectors at the DuPont-Northwestern-Dow (DND) SID-D beamline located at the Advanced Photon Source (APS) of ANL. Data were collected at an incident photon energy of 16.00 keV at room temperature. The powdered Pd/STO samples were loaded into Kapton capillary tubes of 1.1 mm in diameter (Cole-Parmer). SAXS data were also taken from an empty capillary tube for background subtraction. During the measurements, five images were taken for each sample, and the exposure time for each image was 0.1 s. The 2D SAXS patterns were converted to 1D intensity profiles and were averaged together.

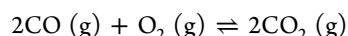
**2.2.3. Inductively Coupled Plasma Atomic Emission Spectroscopy (ICP-AES) and X-ray fluorescence (XRF).** The weight percent (wt %) and coverage (atoms/nm<sup>2</sup>) of Pd were obtained by using both inductively coupled plasma atomic emission spectroscopy (ICP-AES, or ICP) and X-ray fluorescence (XRF). The ICP measurements were conducted at the Quantitative Bio-element Imaging Center at NU. The Pd/STO samples were dissolved in aqua regia at room temperature for 24 h prior to ICP measurements. The wt % Pd and BET surface area of the STO nanopolyhedra were used to calculate the coverage of Pd by assuming stoichiometric SrTiO<sub>3</sub> nanopolyhedra. The XRF measurements were performed at the APS DND 5BM-D beamline. Data were collected at an incident photon energy of 24.40 keV by two Vortex-ME4 four-element silicon drift detectors (SDD). The atomic ratio between Pd and Sr was obtained from XRF data and converted to wt % Pd by assuming stoichiometric SrTiO<sub>3</sub>. The coverage of Pd on the STO support was calculated accordingly from the Pd/Sr atomic ratio and BET surface area of the STO nanopolyhedra. (see the [Supporting Information](#) for details in the measurements and calculation.)

**2.2.4. X-ray Absorption Near Edge Structure (XANES).** The chemical states of the supported Pd were determined by measuring the Pd K-edge (24.35 keV) X-ray absorption near edge structure (XANES) measurements. The XANES spectra were measured at the 5BM-D beamline of the APS. The powder Pd/STO samples were uniformly spread onto X-ray transparent tape (3M) and measured in fluorescence mode at room temperature. The XANES data were analyzed using the ATHENA software package.<sup>55</sup>

**2.2.5. Metal Dispersion.** The metal dispersions of the supported Pd nanoparticles were obtained from both the average Pd nanoparticle size<sup>56</sup> and the CO pulse chemisorption method (see [Supporting Information](#) for details). The CO pulse chemisorption measurements were carried out by using an Altamira AMI-200 catalyst characterization instrument in the

Clean Catalysis (CleanCat) Core facility at NU. The Pd/STO catalysts were prereduced by 10% H<sub>2</sub>/Ar at 360 °C for 300 min, followed by 25 pulses of 1 or 2.5% CO/He injections at room temperature.

**2.3. Catalytic Performance Testing.** To determine the catalytic activity of the Pd/STO samples, the CO oxidation reaction



was employed using a premixed 0.5% CO/20% O<sub>2</sub>/He reactant gas. The gas-phase reactions were performed using a BenchCAT 4000 reactor system (Altamira Instruments) in the CleanCat Core facility at NU. The system used a 1/4" diameter vertical quartz tube flow reactor. In a typical run, approximately 50 mg of the catalyst was blended with 300 mg of SiO<sub>2</sub> powder (Sigma-Aldrich). The catalyst bed was supported on a quartz wool bed. A CO oxidation catalytic run consisted of varying the reaction gas flow rate from 50 to 200 standard cubic centimeters per minute (sccm), consecutively at 80, 100, and 120 °C. The conversion of CO was measured using an Agilent 6850 Gas Chromatograph. All reaction runs were repeated at least three times, and the average values of CO conversion were obtained with standard deviations. The performance of the Pd/STO samples was evaluated using the turnover frequency (TOF) of the CO oxidation reaction. TOF was defined as the frequency of CO conversion per surface Pd, in units of s<sup>-1</sup>.

**2.4. Diffuse Reflectance Infrared Fourier Transform Spectroscopy (DRIFTS).** The DRIFTS measurements were carried out using a Thermal 6700 FTIR in the CleanCat Core facility at NU. For a typical experiment, 80–100 mg of pure SiO<sub>2</sub> powder (Sigma-Aldrich) was loaded into a Praying Mantis cell. A total of 20–25 mg of the Pd/STO catalyst was packed on top of the SiO<sub>2</sub>. The catalyst was reduced in 150 sccm of 10% H<sub>2</sub>/Ar flow at 300 °C for 30 min to remove Pd oxide on the surface due to air exposure and then purged with pure Ar before measurement. The background spectrum was collected at room temperature under constant Ar gas flow. The Pd/STO sample was saturated in 5% CO/He gas flow for at least 10 min, followed by an Ar gas purge at 30–60 sccm. The DRIFTS measurements were collected every minute at room temperature in a mixture of 1.5 sccm O<sub>2</sub> and 25.5 sccm Ar flow.

### 3. RESULTS AND DISCUSSION

**3.1. Morphology.** The Figure 1 TEM images show that Pd deposited by 1 to 10 cycles of ALD forms uniformly dispersed NPs, decorating the surfaces of both types of STO nanopolyhedra used in this study. The NPs exhibit approximately equiaxed shapes with narrow size distributions, ranging from 2–3 nm, as shown in Figure 2. Though the size and number of the ALD-Pd both increase as the number of ALD cycles goes up, these two features grow with different rates. When the number of ALD cycles increases, Pd on the TiO<sub>2</sub>-(001) surface follows the nucleation and growth model, as previously observed for ALD-Pt<sup>40</sup> and ALD-Pd<sup>42</sup> on the same type of STO surface. For this case, the increase in Pd size is more predominant than that in number. In contrast, Pd NPs on the (110)-STO surface from 1c to 5c grow significantly in number, while the growth of size is not as significant. This trend suggests that secondary nucleation<sup>57,58</sup> occurs on the (110)-STO surface in subsequent ALD cycles. The number density of Pd from 5c to 10c, however, does not change significantly (see Supporting Information). Note that for 1, 5, and 10 ALD cycles, the

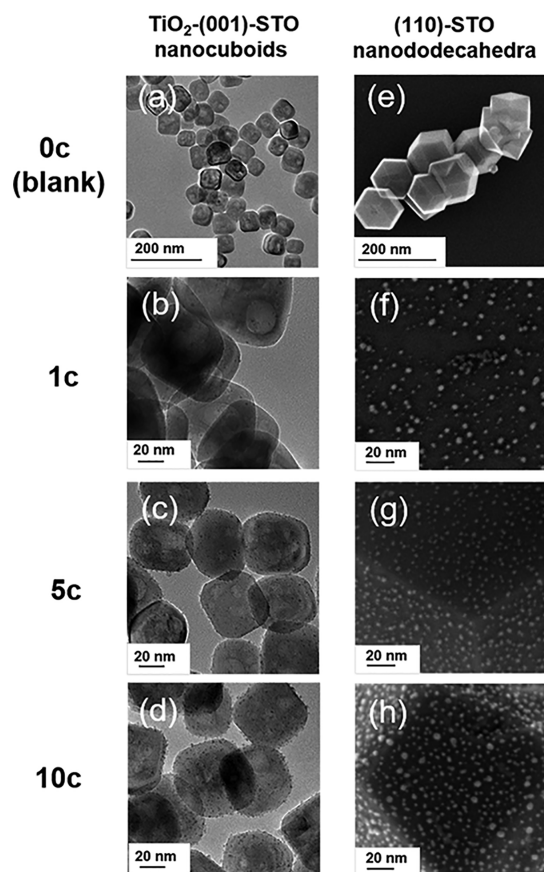


**Figure 1.** TEM images of ALD-Pd deposited on STO nanopolyhedra supports. The left column shows the bright field images of (a) 0c (blank STO), (b) 1c, (c) 5c, and (d) 10c of Pd loaded on the TiO<sub>2</sub>-(001)-STO nanocuboid support. The right column shows the secondary electron images of (e) 0c, (f) 1c, (g) 5c, and (h) 10c of Pd loaded on the (110)-STO nanododecahedra support.

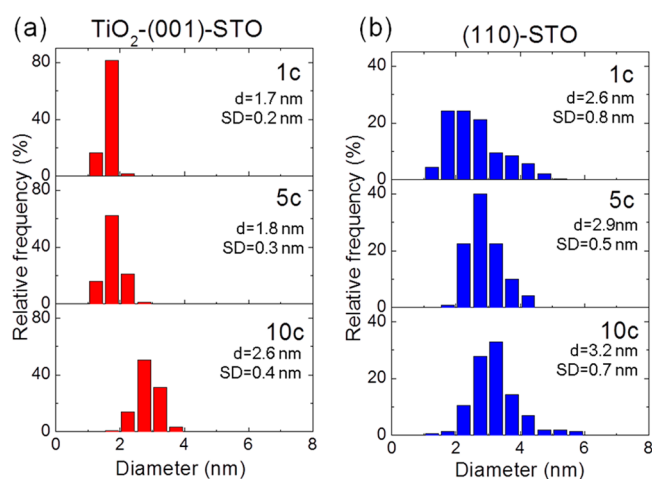


**Figure 2.** Histograms of Pd nanoparticle diameters obtained from multiple representative TEM images: (a) 1c, 5c, and 10c Pd/TiO<sub>2</sub>-(001)-STO nanocuboids, and (b) 1c, 5c, and 10c Pd/(110)-STO nanododecahedra. The mean diameters (*d*) and standard deviations (SD) are included.

average diameters of Pd NPs on (110)-STO surfaces are larger than on TiO<sub>2</sub>-(001)-STO surfaces.

To obtain morphological information as a representative global average, SAXS measurements were implemented to

complement the local structure resolved from TEM. Figure 3a and b show the background subtracted SAXS data of Pd on

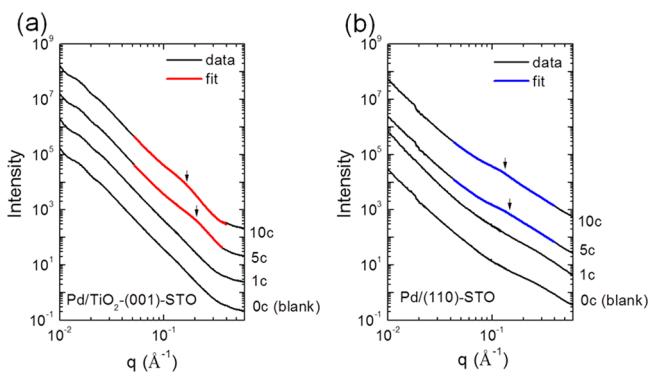


**Figure 3.** Background subtracted SAXS data of (a) Pd/TiO<sub>2</sub>-(001)-STO and (b) Pd/(110)-STO samples (offset for clarity). The interference between neighboring Pd nanoparticles leads to a broad peak in the range of  $q = 0.1\text{--}0.3 \text{ \AA}^{-1}$ . The position of the interference peak ( $q_p$ ) is obtained by fitting the peak with a Gaussian function on a power-law background (see Supporting Information for details in fitting). As indicated by the arrows,  $q_p$  shifts to a lower  $q$  region as the number of ALD cycles increases.

TiO<sub>2</sub>-(001)-STO nanocuboids and (110)-STO nanododecahedra, respectively. For both supports, broad peaks are observed in the range  $q = 0.1\text{--}0.3 \text{ \AA}^{-1}$ , which is due to constructive interference between neighboring Pd nanoparticles and is related to the average interparticle spacing ( $D$ ) as  $D = 2\pi/q_p$ . The peak position  $q_p$  shifts to lower  $q$  as the number of ALD cycles increases. The fitted position of  $q_p$  and the corresponding  $D$  values are summarized in Table 1 (see Supporting Information for fitting details).

**Table 1. Fitted Interparticle Spacing ( $D$ ) from the SAXS Results in Figure 3**

	TiO <sub>2</sub> -(001)-STO		(110)-STO	
	$q_{\text{peak}} (\text{\AA}^{-1})$	$D$ (nm)	$q_{\text{peak}} (\text{\AA}^{-1})$	$D$ (nm)
1c <sup>a</sup>				
5c	0.22(1)	2.9(2)	0.15(1)	4.5(3)
10c	0.16(1)	3.7(2)	0.13(1)	4.9(4)

<sup>a</sup>Meaningful fitting results were unobtainable from the 1c samples due to the weak intensity of the interference peak.

The SAXS result shows that average NP separation distance  $D$  is generally larger on the (110)-STO surface than that on the TiO<sub>2</sub>-(001)-STO surface. From 5c to 10c,  $D$  increases from 2.9 to 3.7 nm on the TiO<sub>2</sub>-(001)-STO surface, while  $D$  only slightly increases from 4.4 to 4.9 nm on (110)-STO nanododecahedra. The larger fractional increase in  $D$  for the TiO<sub>2</sub>-(001)-STO surface implies coalescence between Pd nanoparticles, consistent with the TEM observed nucleation and growth process. A similar coalescence trend was reported in ref 40 for ALD-Pt on the same type of TiO<sub>2</sub>-(001)-STO nanocuboids. For Pd on the (110)-STO surface, the slight increase in  $D$  is consistent with the insignificant variation in the number density of Pd.

How the density of nanoparticles and size grow with the number of deposition cycles depends upon competition between three factors: the relative binding of precursors on the oxide versus the nanoparticle, surface diffusion of the metal

atoms across the surface, the critical nucleus size, and the specific surface termination; see, for instance, refs 41, 59, and 60 and references therein. The TiO<sub>2</sub>-(001) terminated SrTiO<sub>3</sub> has octahedral terminated TiO<sub>5</sub>□ units (where □ is a vacant site) with a  $\sqrt{13} \times \sqrt{13}$  reconstructed surface,<sup>43,61,62</sup> whereas the (110)-STO dodecahedra have tetrahedral TiO<sub>4</sub> surface terminations.<sup>39,63</sup> All the terms, which control the growth trajectory of the nanoparticles, will be completely different for the two surfaces; they have fundamentally different chemistries so STO nanoparticles with just TiO<sub>2</sub>-(001) versus (110) surfaces should be considered as effectively different compounds. As a result, it is to be expected that there will be significant variations in the growth rate and the change in nanoparticle size and density for the different supports. The relatively small change in the number density on the TiO<sub>2</sub>-(001) surfaces indicates that some combination of a faster surface diffusion rate and/or a larger critical nucleus size dominates. Therefore, during additional ALD cycles, the Pd atoms strongly tend to add to existing nuclei. In contrast, for the (110)-STO surface, the change in the number of nuclei with time implies a lower surface diffusion rate and/or a smaller critical nucleus size, so additional secondary nucleation is taking place.

**3.2. Multiply Twinned Pd Nanoparticles.** In previous, comparable work for Pt NPs on STO<sup>8,9</sup> and Ba<sub>0.5</sub>Sr<sub>0.5</sub>TiO<sub>3</sub>,<sup>44</sup> the particles were >99% single crystals with a cube-on-cube epitaxy to the TiO<sub>2</sub>-rich (001) surface. These showed a small, but significant, difference in the adhesion measurable using a Winterbottom construction<sup>45</sup> that led to significant changes in the catalysis.<sup>8,44</sup> The Pd NPs here were more complex. All FCC metals can form multiply twinned particles (MTPs),<sup>48–53</sup> which can have lower total energy due to more {111} surfaces at the expense of internal strains;<sup>64</sup> see ref 53 and references therein for more details. While MTPs do have preferable, epitaxial orientations on substrates as demonstrated in the original work,<sup>48</sup> this is complicated by the presence of twinning. While parts of the NPs can form low-energy interfaces with the oxide support, this is disrupted by the change in orientation due to the twins.

This twinning effect is reflected in our results. Figure 4 shows atomic resolution images of individual Pd NPs supported on the surfaces of TiO<sub>2</sub>-(001)-STO nanocuboids and (110)-STO nanododecahedra. The Pd NPs are crystalline with faceted geometry. Figure 4 also shows a range of observed Pd NP shapes, including representative single crystals and multiply twinned Pd NPs on both STO surfaces, with approximately 70% of the NPs being MTPs, and 30% single crystals. While the minority single crystals tend to show quite strong adhesion, the majority MTPs has much weaker adhesion energy. This adhesion energy is reflected in the height of the NPs, as the height of the MTPs is approximately half compared to the Wulff shape of Pd.<sup>53</sup>

Because of this weak adhesion, the substrate plays little to no role in determining the exposed facets of the nanoparticles. For completeness, while the presence of MTPs has long been speculated to perhaps play a role in changing the catalytic performance (e.g., refs 65 and 66), we have no evidence to show that they play any significant role here in this study. As will be seen later, the catalytic performance is dominated by the coverage of CO, rather than the NP shape and epitaxy in this case.

**3.3. Loading and Coverage.** The weight percent (wt %) loading of Pd was obtained by using both ICP and XRF, as

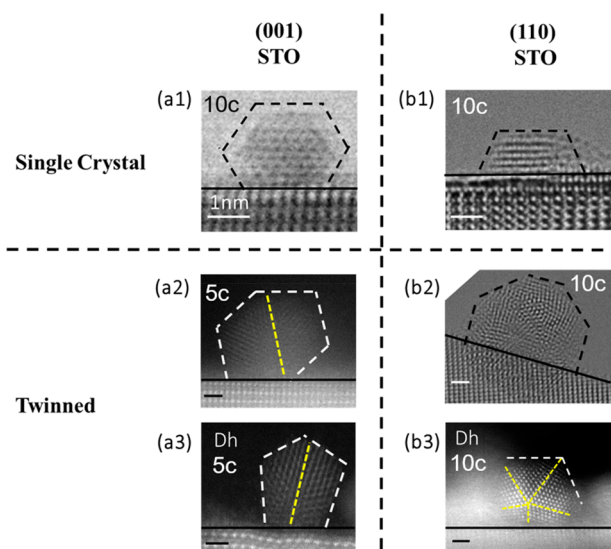


**Figure 4.** High resolution images showing Pd NPs supported on the  $\text{TiO}_2$ -(001)-STO and (110)-STO surfaces. The numbers of ALD cycles are marked in each of the images. The scale bar (1 nm) applies to all images. On the two types of STO surfaces, single (a1, b1) and twinned (a2, a3, b2, and b3) Pd NPs coexist. The images also show Pd NPs with a variety of shapes, which are outlined with the white dashed lines. The twin boundaries, where identifiable, are represented by the yellow dashed lines. The images are from TEM in a1 and a2, annular bright field (ABF) in b1, and high angle annular dark field (HAADF) in b2, b3, and a3, respectively.

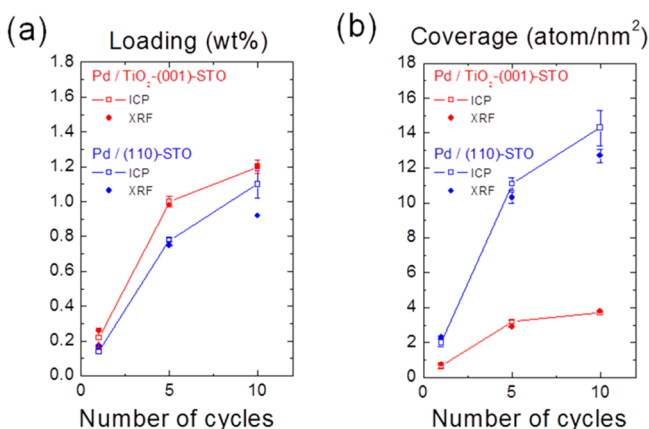


**Figure 5.** (a) Wt% loading of Pd and (b) Pd surface coverage as a function of the number of ALD cycles calculated from both XRF and ICP measurements. The red line and the blue line represent Pd/ $\text{TiO}_2$ -(001)-STO and Pd/(110)-STO, respectively. The coverage is defined as the surface density of Pd atoms and assumes all Pd are on the STO support surface. The numerical data of wt % and coverage are presented in Table 2.

shown in Figure 5a (the details are summarized in Table 2). However, as the two types of STO nanopolyhedra supports have different surface-to-volume ratios, the Pd loading on each support cannot be compared directly by using wt %. Instead, we use “coverage,” defined as the density of Pd atoms per unit surface area of the nanopolyhedra ( $\text{atom}/\text{nm}^2$ ) to exclude the volume effect. Figure 5b displays the calculated Pd coverage on the two types of surfaces. Compared to the  $\text{TiO}_2$ -(001)-STO

surface, the growth rate of Pd on (110)-STO surface is approximately 3 times higher.

Pd shows significant mass gain during the initial ALD cycles on both types of supports. The loading increases by approximately 5 times from 1c to 5c, while the mass gain is less significant from 5c to 10c. Furthermore, the mass gain of Pd for the first cycle is the same as the average gain of cycles 2 through 5 (0.20 and 0.16 wt % per cycle on  $\text{TiO}_2$ -(001)-STO nanocuboids and (110)-STO nanododecahedra, respectively), implying a linear growth from 1c to 5c Pd on both types of STO nanopolyhedra. The linear mass gain of Pd for the initial ALD cycles is analogous to the earlier study of Pt-ALD on  $\text{TiO}_2$ -(001)-STO nanocuboids.<sup>40</sup> Nevertheless, the mass gain per ALD cycle of Pt is  $\sim 20$  times higher on  $\text{TiO}_2$ -(001)-STO nanocuboids (corresponding to  $\sim 10$  times higher in coverage per cycle compared to that of Pd). It should be noted that the linear growth model of ALD-Pd observed here deviates slightly from previous results,<sup>8,41</sup> where the growth rate of ALD-Pt is higher for the first cycle than the subsequent cycles.

**3.4. Pd<sup>0</sup> Atomic Fraction.** Figure 6a and b show Pd K-edge XANES of Pd nanoparticles supported on  $\text{TiO}_2$ -(001)-STO nanocuboids and (110)-STO nanododecahedra, respectively. On the two types of STO surfaces, metallic ( $\text{Pd}^0$ ) and oxide ( $\text{Pd}^{2+}$ ) phases of Pd coexist. The oxidation state of Pd shifts gradually from  $\text{Pd}^{2+}$  to  $\text{Pd}^0$  with increased Pd loading. Figure 6c shows the atomic fraction ( $f$ ) of Pd in the  $\text{Pd}^0$  chemical state, which was calculated from the linear combination fitting of the Pd foil and PdO(II) reference spectra under the assumption that  $f_{\text{Pd}^0} + f_{\text{Pd}^{2+}} = 1$ . The result shows that  $f_{\text{Pd}^0}$  increases monotonically with the number of ALD cycles for both supports and is higher on (110)-STO than that on  $\text{TiO}_2$ -(001)-STO for the same number of ALD cycles. A higher  $\text{Pd}^0$  fraction is consistent with larger nanoparticles having a smaller fraction of oxidized atoms at the surface.

**3.5. CO Oxidation Activity.** Figure 7 and Table 3 show the Arrhenius plot and turnover frequency (TOF) of the CO oxidation reaction over 1, 5, and 10c Pd on the two types of STO nanopolyhedra. No major difference was observed in the TOFs for 5c Pd/ $\text{TiO}_2$ -(001)-STO, 10c Pd/ $\text{TiO}_2$ -(001)-STO, 1c Pd/(110)-STO, and 5c Pd/(110)-STO. However, 1c Pd/ $\text{TiO}_2$ -(001)-STO displays 2–3 times higher TOF and a lower apparent activation energy at 80 and 100 °C compared to other samples.

The elevated TOF of 1c Pd/ $\text{TiO}_2$ -(001)-STO was further studied by using DRIFTS measurements of the CO adsorption intensity on Pd under  $\text{O}_2$  exposure. We examined 1c Pd/ $\text{TiO}_2$ -(001)-STO, 10c Pd/ $\text{TiO}_2$ -(001)-STO, and 1c Pd/(110)-STO samples, with average Pd sizes of 1.7, 2.6, and 2.6 nm, respectively. Figure 8a–c are the results of the DRIFTS measurements, showing two groups of CO absorption bands: the linear absorption band ( $\sim 2000$ – $2100 \text{ cm}^{-1}$ , denoted as L sites) and the bridge-multiple absorption band ( $\sim 1800$ – $2000 \text{ cm}^{-1}$ , denoted as B-M sites).<sup>67–69</sup> The broad width of the L and B-M bands indicates the presence of multiple CO adsorption species on the Pd surface.<sup>67</sup> On the basis of the literature, absorption peaks around 1970 and 1923  $\text{cm}^{-1}$  are assigned to compressed bridged (CO/Pd = 1:1.5) and isolated bridged CO (CO/Pd = 1:2) on the Pd surface, respectively.<sup>70,71</sup>

On introduction of  $\text{O}_2$ , CO adsorption intensities for both 10c/ $\text{TiO}_2$ -(001)-STO and 1c/(110)-STO show an abrupt decrease in the presence of  $\text{O}_2$ , while the intensity decay is smoother for 1c/ $\text{TiO}_2$ -(001)-STO, as shown in Figure 8d,e. The abrupt decrease in intensity occurs for larger Pd NPs (2.6

**Table 2. Atomic Ratio of Pd to Sr, Pd Loading (wt%), and Pd Coverage**

termination	cycles	Pd/Sr atomic ratio		Pd loading (wt %)		Pd coverage (atom/nm <sup>2</sup> ) <sup>c</sup>	
		XRF	ICP <sup>a</sup>	XRF <sup>b</sup>	ICP	XRF	ICP
TiO <sub>2</sub> -(001)-STO	1c	0.0045	0.004(1)	0.26	0.22(6)	0.8(1)	0.7(2)
	5c	0.017	0.019(1)	0.99	1.00(3)	2.9(1)	3.2(1)
	10c	0.019	0.022(1)	1.20	1.20(4)	3.2(1)	3.7(1)
(110)-STO	1c	0.0029	0.0025(2)	0.17	0.14(2)	2.3(1)	2.0(2)
	5c	0.013	0.014(1)	0.75	0.78(1)	10.3(3)	11.1(4)
	10c	0.016	0.017(1)	0.92	1.10(7)	12.7(4)	14(1)

<sup>a</sup>Calculated from ICP obtained wt % Pd and wt % Sr assuming stoichiometric SrTiO<sub>3</sub> nanopolyhedra. <sup>b</sup>Calculated from Pd/Sr atomic ratio assuming stoichiometric SrTiO<sub>3</sub>. The XRF error is small (<1%) due to good counting statistics. <sup>c</sup>Calculated from Pd/Sr atomic ratio and BET surface areas of the two types of STO nanopolyhedra supports.

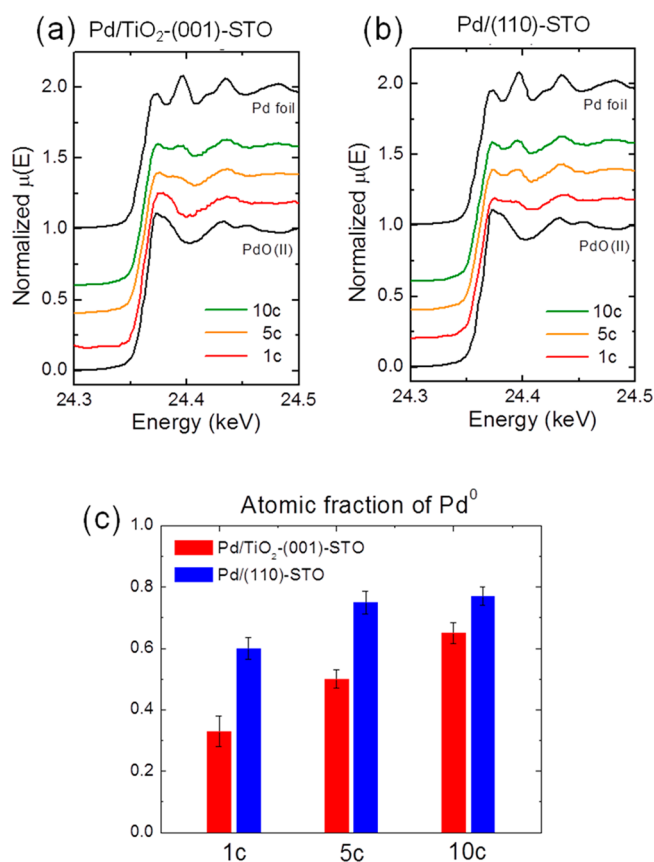


**Figure 6.** Pd K-edge XANES of (a) Pd/TiO<sub>2</sub>-(001)-STO nanocuboids and (b) Pd/(110)-STO nanododecahedra. The Pd foil (Pd<sup>0</sup>) and PdO(II) (Pd<sup>2+</sup>) spectra are shown as references. Comparing the data to the references reveals that the chemical state of supported Pd NPs gradually shifts from Pd<sup>2+</sup> to Pd<sup>0</sup> as the loading increases. (c) The atomic fraction of metallic Pd ( $f_{\text{Pd}^0}$ ) obtained from linear combination fitting.  $f_{\text{Pd}^0}$  is higher on (110)-STO than on the TiO<sub>2</sub>-(001)-STO surface at the same number of ALD cycles.

nm) but not for smaller Pd NPs (1.7 nm). Note that the compressed bridging peak, which is only seen in the 10c/TiO<sub>2</sub>-(001)-STO and 1c/(110)-STO, vanishes upon oxidation, as shown in Figure 8b and c. The isolated bridging peak in the 1c/TiO<sub>2</sub>-(001)-STO in Figure 8a, however, remains present even after a long exposure to O<sub>2</sub>. The difference in surface CO coverage may explain the difference in TOF between 1c/TiO<sub>2</sub>-(001)-STO and the other two Pd/STO catalysts.

The delayed onset and abrupt decrease in the DRIFTS intensity during CO oxidation is attributed to CO inhibiting the initial adsorption on the larger Pd nanoparticles. It is well-

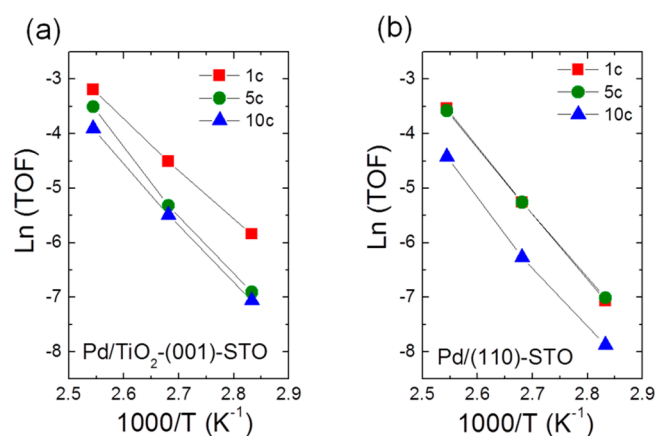
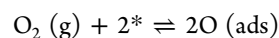
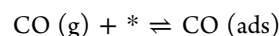


**Figure 7.** Arrhenius plots for the CO oxidation reaction of (a) Pd/TiO<sub>2</sub>-(001)-STO and (b) Pd/(110)-STO. The 1c Pd/TiO<sub>2</sub>-(001)-STO sample is more active than the others and has lower apparent activation energy, as indicated by the smaller absolute value of the slope. The turn over frequency (TOF) of individual samples can be found in Table 3.

established that the CO oxidation reaction over Pd surfaces follows the Langmuir–Hinshelwood reaction mechanism.<sup>72–75</sup> In this mechanism, the adsorption of CO and O<sub>2</sub> molecules involves the following elementary steps (\* denotes a free adsorption site):



It is known that O<sub>2</sub> possesses a lower sticking coefficient than CO on Pd surfaces, and the sticking coefficient drops as CO coverage increases.<sup>76–78</sup> Due to CO occupying the Pd surface, the initial CO<sub>2</sub> production rate is slow because O<sub>2</sub> adsorption is inhibited. The influence of the unequal adsorption strengths was previously demonstrated by studies exposing O<sub>2</sub> on Pd single crystal surfaces<sup>76</sup> and nanoparticles,<sup>75,77</sup> both precovered with CO.

The CO coverage effect described above may occur in our Pd/STO samples with larger Pd NP size, where there are more facet sites than corner/edge sites. Initially, the dissociative adsorption of O<sub>2</sub> is inhibited by CO covered Pd facets. Then, successful adsorption of O<sub>2</sub> on some unoccupied adsorption sites allows CO in the vicinity of the adsorbed O<sub>2</sub> to be consumed. This creates additional adsorption sites for O<sub>2</sub> molecules. Because the presence of the active O<sub>2</sub> species accelerates the CO<sub>2</sub> production rate when the surface coverage of CO is high, the intensity of CO adsorption bands in DRIFTS

Table 3. CO Oxidation Turnover Frequency (TOF) at 80–120 °C for the Pd/STO Catalysts<sup>a</sup>

support	# cycles	diameter (nm) <sup>b</sup>	standard deviation <sup>c</sup> (nm)	dispersion (%) <sup>d</sup>	TOF 80 °C (s <sup>-1</sup> )	TOF 100 °C (s <sup>-1</sup> )	TOF 120 °C (s <sup>-1</sup> )	apparent activation energy (kJ/mol)
TiO <sub>2</sub> -(001)-STO nanocuboids	1c	1.7	0.2	73.8	2.9(1) × 10 <sup>-3</sup>	1.1(1) × 10 <sup>-2</sup>	4.1(4) × 10 <sup>-2</sup>	76.3
	5c	1.8	0.3	69.7	1.0(1) × 10 <sup>-3</sup>	4.9(2) × 10 <sup>-3</sup>	3.0 × 10 <sup>-2</sup>	97.9
	10c	2.6	0.4	48.2	8.5(5) × 10 <sup>-4</sup>	4.1(3) × 10 <sup>-3</sup>	2.1(3) × 10 <sup>-2</sup>	90.8
(110)-STO nanododecahedra	1c	2.6	0.8	48.2	8.5(4) × 10 <sup>-4</sup>	5.2(5) × 10 <sup>-3</sup>	2.9(3) × 10 <sup>-2</sup>	101.6
	5c	2.9	0.5	43.2	9(1) × 10 <sup>-4</sup>	5.1(6) × 10 <sup>-3</sup>	2.8(2) × 10 <sup>-2</sup>	99.0
	10c	3.2	0.7	39.2	3.8 × 10 <sup>-4</sup>	1.9 × 10 <sup>-3</sup>	1.2 × 10 <sup>-2</sup>	99.3

<sup>a</sup>TOF was calculated from ICP obtained wt % and TEM estimated metal dispersion (see [Support Information](#) for details). <sup>b</sup>Average diameter of Pd obtained from multiple TEM images. <sup>c</sup>Standard deviation of Pd NP diameter. <sup>d</sup>Dispersion estimated from the average diameter of Pd.

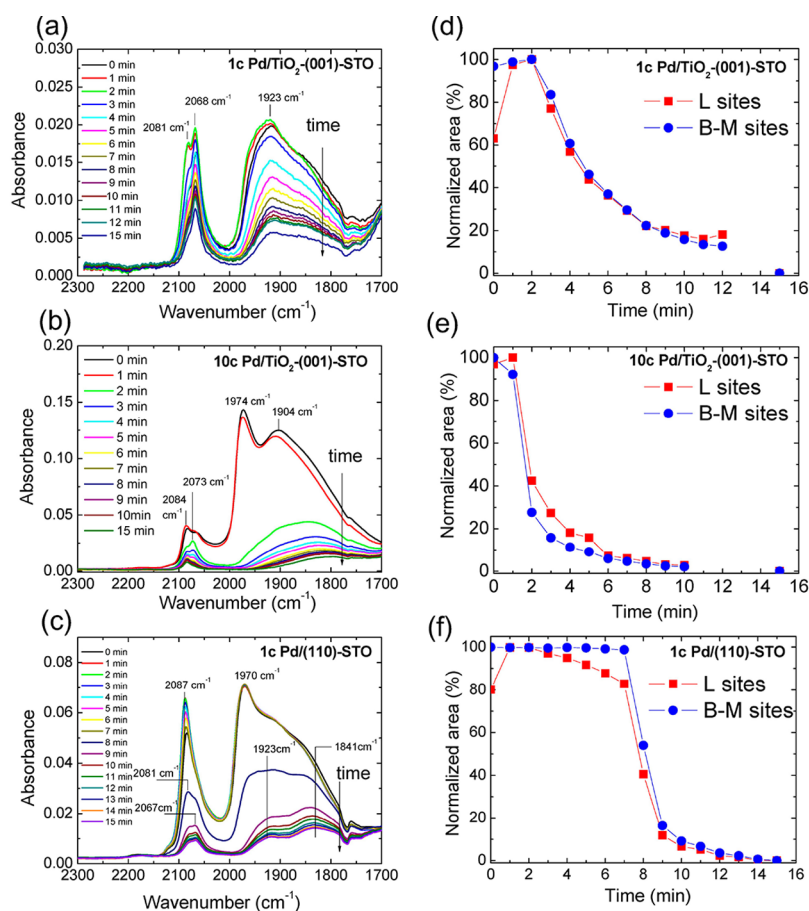


**Figure 8.** DRIFTS showing CO absorption intensity as a function of O<sub>2</sub> exposure time at room temperature for (a) 1c Pd/TiO<sub>2</sub>-(001)-STO nanocuboids, (b) 10c Pd/TiO<sub>2</sub>-(001)-STO nanocuboids, and (c) 1c Pd/(110)-STO nanododecahedra. (d–f) The evolution of normalized CO adsorption peak areas over time. The area denoted as L sites is the linear absorption branch (~2000–2100 cm<sup>-1</sup>), and the bridge-multiple branch (~1800–2000 cm<sup>-1</sup>) is denoted as B-M sites.

drops dramatically due to fast CO consumption. This phenomenon was also observed in many empty adsorption site (or vacancy) mediated surface autocatalytic reaction processes.<sup>72,79,80</sup>

However, 1c Pd/TiO<sub>2</sub>-(001)-STO has smaller Pd NPs (~2 nm), on which the CO coverage effect is less prominent due to the larger fraction of the Pd edge/corner sites. These low coordinated sites result in stronger O<sub>2</sub> adsorption/dissociation.<sup>78</sup> As a consequence, O<sub>2</sub> dissociates on Pd and reacts with CO more easily, causing a steady decrease in the CO adsorption intensity. The isolated bridged CO, as shown in [Figure 8a](#), also supports the existence of extra O<sub>2</sub> adsorption sites due to the lower coverage of CO on 1c Pd/TiO<sub>2</sub>-(001)-STO. This argument explains the significantly higher TOF of

1c Pd/TiO<sub>2</sub>-(001)-STO compared to the other samples, because the reaction is not inhibited due to the lower coverage of CO. At 120 °C, the TOF of 1c Pd/TiO<sub>2</sub>-(001)-STO and other samples are similar due to the weakened adsorption strength of CO, which decreases the effect of CO coverage. Additionally, raising the temperature increases the overall rate of the CO oxidation reaction.

Also note that the concerted decrease of the CO absorption intensity for the L sites and B-M sites shown in [Figure 8d–f](#) is consistent for all three samples investigated. [Figure 9](#) shows that the area ratios of B-M to L sites of 1c Pd/(110)-STO and 1c Pd/TiO<sub>2</sub>-(001)-STO remain constant during the O<sub>2</sub> exposure. For 10c Pd/TiO<sub>2</sub>-(001)-STO, while there is a sharp drop in the B-M/L ratio during the initial 2 min, the ratio

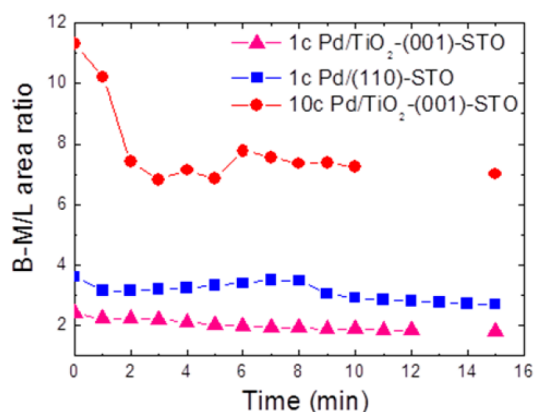


**Figure 9.** Evolution of the B-M to L area ratios with O<sub>2</sub> exposure time. The B-M to L ratios stay constant for the three samples, indicating the redistribution of CO adsorption sites as CO is removed.

also becomes constant after the drop. The constant ratio during O<sub>2</sub> exposure for individual samples indicates that the adsorbed CO migrates over the Pd surface and redistributes as CO is removed.

Note that the B-M/L ratio for 10c Pd/TiO<sub>2</sub>-(001)-STO is the highest among the three samples shown in Figure 9. The high B-M/L ratio can be explained by the size of Pd NPs. Compared to 1c Pd/TiO<sub>2</sub>-(001)-STO (1.7 nm diameter), 10c Pd/TiO<sub>2</sub>-(001)-STO is larger in size (2.6 nm) and thus has a higher fraction of facet sites.<sup>67,68</sup> For the 1c Pd/(110)-STO sample, although the average Pd diameter (2.6 nm) is the same as that of 10c Pd/TiO<sub>2</sub>-(001)-STO, its size distribution is skewed to smaller sizes (~25% of the NPs are smaller than 2 nm, as shown in Figure 2). Therefore, the B-M/L ratio is lower than the 10c Pd/TiO<sub>2</sub>-(001)-STO due to the smaller NPs.

#### 4. SUMMARY AND CONCLUSION

This work investigates the morphology and CO oxidation activity of uniformly distributed ALD-Pd NPs supported on single crystal TiO<sub>2</sub>-(001)-STO nanocuboids and (110)-STO nanododecahedra. ALD demonstrated controlled growth of Pd. The deposition rate of Pd is higher from 1c to 5c than 5c to 10c on both of the STO surfaces and is three times higher on the (110)-STO nanododecahedra than on the TiO<sub>2</sub>-(001)-STO nanocuboids. As Pd loading increases, Pd on the TiO<sub>2</sub>-(001)-STO surface follows the nucleation and growth model and grows more significantly in size compared to that in number, while Pd on the (110)-STO surface begins with secondary nucleation and grows more in number than in size. On both types of STO surfaces, approximately 30% of the Pd NPs are single crystal and 70% are multiply twinned. The Pd NPs show varieties of shapes, degrees of wetting, and interface orientations. Whether MTPs or single crystals are formed has a complex dependence upon the method of preparation and surface chemisorption;<sup>53</sup> therefore, there may be other ways of preparing the Pd so stronger epitaxial effects will be observed. In this particular system, the surface orientation of the STO support is not a determining factor in CO oxidation reaction because of the weak adhesion between the Pd and STO for the majority MTPs. Nevertheless, TOF analysis and DRIFTS show that the CO oxidation activity is mostly dominated by the Pd size due to CO coverage effects. For larger Pd nanoparticles, CO oxidation activity is lower because of the higher CO coverage on the relatively higher proportion of facet sites,

which causes inhibited O<sub>2</sub> adsorption. In contrast, the smaller Pd nanoparticles have a higher proportion of edge and corner sites, allowing dissociative adsorption of O<sub>2</sub> on these sites and leading to higher CO oxidation activity.

#### ■ ASSOCIATED CONTENT

##### Supporting Information

The Supporting Information is available free of charge on the ACS Publications website at DOI: 10.1021/acscatal.7b04173.

Detailed data analysis procedure, including the X-ray measurements setup and data analysis, calculation of the CO oxidation turnover frequency, and analysis of high-resolution electron microscopy images (PDF)

#### ■ AUTHOR INFORMATION

##### Corresponding Author

\*E-mail: bedzyk@northwestern.edu.

##### ORCID

Lawrence A. Crosby: 0000-0001-7644-3762

Robert M. Kennedy: 0000-0001-6836-7923

Richard P. Van Duyne: 0000-0001-8861-2228

Kenneth R. Poeppelmeier: 0000-0003-1655-9127

Michael J. Bedzyk: 0000-0002-1026-4558

##### Notes

The authors declare no competing financial interest.

#### ■ ACKNOWLEDGMENTS

This work was supported by the Institute for Catalysis in Energy Processes (ICEP) at Northwestern University (NU) under DOE Grant DE-FG02-03ER15457. X-ray measurements were performed at the Advanced Photon Source of Argonne National Lab (ANL), at DND-CAT (Sector 5), which is supported by E.I. DuPont de Nemours & Co., NU, and The Dow Chemical Co. ANL is supported by DOE under grant number DE-AC02-06CH11357. We thank Qing Ma and Steve Weigand at DND-CAT for assisting with the XANES and SAXS measurements. Electron microscopy was performed at the EPIC facility supported by the NU-MRSEC program (NSF DMR-1720139) and at the UIC Research Resources Center supported by an MRI-R<sup>2</sup> grant from the National Science Foundation (NSF DMR-0959470). Use of aberration-corrected TEM at the Center for Nanoscale Materials, an Office of Science user facility, was supported by the U.S. Department of Energy, Office of Science, Office of Basic Energy Sciences, under Contract No. DE-AC02-06CH11357. The TOF analysis and DRIFTS were performed at the Clean Catalysis Core facility, which acknowledges funding from the Department of Energy (DE-FG02-03ER15457 and DE-AC02-06CH11357) used for the purchase of the Thermo 6700 DRIFTS system and the Altamira AMI-200. ICP-AES measurements were performed at the Northwestern University Quantitative Bioelement Imaging Center. B.R.C. was partially supported by Study Abroad Fellowship from Ministry of Education of Taiwan. L.A.C. is supported by a National Science Foundation Graduate Research Fellowship.

#### ■ REFERENCES

- (1) Tauster, S. J. Strong Metal-Support Interactions. *Acc. Chem. Res.* 1987, 20, 389–394.
- (2) Willinger, M. G.; Zhang, W.; Bondarchuk, O.; Shaikhutdinov, S.; Freund, H. J.; Schlogl, R. A Case of Strong Metal-Support

Interactions: Combining Advanced Microscopy and Model Systems to Elucidate the Atomic Structure of Interfaces. *Angew. Chem., Int. Ed.* **2014**, *53*, 5998–6001.

(3) Fu, Q.; Wagner, T. Interaction of nanostructured metal overlayers with oxide surfaces. *Surf. Sci. Rep.* **2007**, *62*, 431–498.

(4) Freund, H. J.; Nilius, N.; Risse, T.; Schauermaun, S. A fresh look at an old nano-technology: catalysis. *Phys. Chem. Chem. Phys.* **2014**, *16*, 8148–8167.

(5) Schubert, M. M.; Hackenberg, S.; van Veen, A. C.; Muhler, M.; Plzak, V.; Behm, R. J. CO oxidation over supported gold catalysts—"inert" and "active" support materials and their role for the oxygen supply during reaction. *J. Catal.* **2001**, *197*, 113–122.

(6) Widmann, D.; Behm, R. J. Activation of Molecular Oxygen and the Nature of the Active Oxygen Species for CO Oxidation on Oxide Supported Au Catalysts. *Acc. Chem. Res.* **2014**, *47*, 740–749.

(7) An, K.; Alayoglu, S.; Musselwhite, N.; Plamthottam, S.; Melaet, G.; Lindeman, A. E.; Somorjai, G. A. Enhanced CO Oxidation Rates at the Interface of Mesoporous Oxides and Pt Nanoparticles. *J. Am. Chem. Soc.* **2013**, *135*, 16689–16696.

(8) Enterkin, J. A.; Setthapun, W.; Elam, J. W.; Christensen, S. T.; Rabuffetti, F. A.; Marks, L. D.; Stair, P. C.; Poepplmeier, K. R.; Marshall, C. L. Propane Oxidation over Pt/SrTiO<sub>3</sub> Nanocuboids. *ACS Catal.* **2011**, *1*, 629–635.

(9) Enterkin, J. A.; Poepplmeier, K. R.; Marks, L. D. Oriented Catalytic Platinum Nanoparticles on High Surface Area Strontium Titanate Nanocuboids. *Nano Lett.* **2011**, *11*, 993–997.

(10) Ertl, G. Elementary Steps in Heterogeneous Catalysis. *Angew. Chem., Int. Ed. Engl.* **1990**, *29*, 1219–1227.

(11) Campbell, C. T. Ultrathin metal films and particles on oxide surfaces: Structural, electronic and chemisorptive properties. *Surf. Sci. Rep.* **1997**, *27*, 1–111.

(12) Henry, C. R. Surface studies of supported model catalysts. *Surf. Sci. Rep.* **1998**, *31*, 231–325.

(13) Baumer, M.; Freund, H. J. Metal deposits on well-ordered oxide films. *Prog. Surf. Sci.* **1999**, *61*, 127–198.

(14) Somorjai, G. A.; McCrea, K. R.; Zhu, J. Active sites in heterogeneous catalysis: development of molecular concepts and future challenges. *Top. Catal.* **2002**, *18*, 157–166.

(15) Gao, F.; Goodman, D. W. Model Catalysts: Simulating the Complexities of Heterogeneous Catalysts. *Annu. Rev. Phys. Chem.* **2012**, *63*, 265–286.

(16) Freund, H. J. Models for heterogeneous catalysts: studies at the atomic level. *Rend. Fis. Acc. Lincei* **2017**, *28*, 5.

(17) Goodman, D. W. Catalysis: from Single-Crystals to the Real World. *Surf. Sci.* **1994**, *299* (1–3), 837–848.

(18) Goodman, D. W. Correlations between Surface Science Models and "Real-World". *J. Phys. Chem.* **1996**, *100*, 13090–13102.

(19) St. Clair, T. P.; Goodman, D. W. Metal nanoclusters supported on metal oxide thin films: bridging the materials gap. *Top. Catal.* **2000**, *13*, 5–19.

(20) Freund, H. J.; Kuhlenbeck, H.; Libuda, J.; Rupprechter, G.; Baumer, M.; Hamann, H. Bridging the pressure and materials gaps between catalysis and surface science: clean and modified oxide surfaces. *Top. Catal.* **2001**, *15*, 201–209.

(21) Somorjai, G. A.; York, R. L.; Butcher, D.; Park, J. Y. The evolution of model catalytic systems; studies of structure, bonding and dynamics from single crystal metal surfaces to nanoparticles, and from low pressure (< 10<sup>−3</sup> Torr) to high pressure (> 10<sup>−3</sup> Torr) to liquid interfaces. *Phys. Chem. Chem. Phys.* **2007**, *9*, 3500–3513.

(22) Carr, R. G.; Somorjai, G. A. Hydrogen-Production from Photolysis of Steam Adsorbed onto Platinized SrTiO<sub>3</sub>. *Nature* **1981**, *290*, 576–577.

(23) Polli, A. D.; Wagner, T.; Gemming, T.; Ruhle, M. Growth of platinum on TiO<sub>2</sub>- and SrO-terminated SrTiO<sub>3</sub>(100). *Surf. Sci.* **2000**, *448*, 279–289.

(24) Iddir, H.; Komanicky, V.; Ogut, S.; You, H.; Zapol, P. Shape of platinum nanoparticles supported on SrTiO<sub>3</sub>: Experiment and theory. *J. Phys. Chem. C* **2007**, *111*, 14782–14789.

(25) Komanicky, V.; Iddir, H.; Chang, K. C.; Menzel, A.; Karapetrov, G.; Hennessy, D.; Zapol, P.; You, H. Shape-Dependent Activity of Platinum Array Catalyst. *J. Am. Chem. Soc.* **2009**, *131*, 5732.

(26) Christensen, S. T.; Elam, J. W.; Lee, B.; Feng, Z.; Bedzyk, M. J.; Hersam, M. C. Nanoscale Structure and Morphology of Atomic Layer Deposition Platinum on SrTiO<sub>3</sub> (001). *Chem. Mater.* **2009**, *21*, 516–521.

(27) Christensen, S. T.; Lee, B.; Feng, Z. X.; Hersam, M. C.; Bedzyk, M. J. Hierarchical nanoparticle morphology for platinum supported on SrTiO<sub>3</sub> (001): A combined microscopy and X-ray scattering study. *Appl. Surf. Sci.* **2009**, *256*, 423–427.

(28) Feng, Z. X.; Christensen, S. T.; Elam, J. W.; Lee, B.; Hersam, M. C.; Bedzyk, M. J. Thermally induced nanoscale structural and morphological changes for atomic-layer-deposited Pt on SrTiO<sub>3</sub>(001). *J. Appl. Phys.* **2011**, *110*, 102202.

(29) Feng, Z. X.; Kazimirov, A.; Bedzyk, M. J. Atomic Imaging of Oxide-Supported Metallic Nanocrystals. *ACS Nano* **2011**, *5*, 9755–9760.

(30) Stoltz, S. E.; Ellis, D. E.; Bedzyk, M. J. Interface of Pt with SrTiO<sub>3</sub>(001); A combined theoretical and experimental study. *Surf. Sci.* **2015**, *633*, 8–16.

(31) Wagner, T.; Richter, G.; Ruhle, M. Epitaxy of Pd thin films on (100) SrTiO<sub>3</sub>: A three-step growth process. *J. Appl. Phys.* **2001**, *89*, 2606–2612.

(32) Silly, F.; Powell, A. C.; Martin, M. G.; Castell, M. R. Growth shapes of supported Pd nanocrystals on SrTiO<sub>3</sub>(001). *Phys. Rev. B: Condens. Matter Mater. Phys.* **2005**, *72*, 165403.

(33) Silly, F.; Castell, M. R. Selecting the shape of supported metal nanocrystals: Pd huts, hexagons, or pyramids on SrTiO<sub>3</sub>(001). *Phys. Rev. Lett.* **2005**, *94* (4), 046103.

(34) Stoltz, S. E.; Ellis, D. E.; Bedzyk, M. J. Structure and reactivity of zero-, two- and three-dimensional Pd supported on SrTiO<sub>3</sub>(001). *Surf. Sci.* **2014**, *630*, 46–63.

(35) Rabuffetti, F. A.; Kim, H. S.; Enterkin, J. A.; Wang, Y. M.; Lanier, C. H.; Marks, L. D.; Poepplmeier, K. R.; Stair, P. C. Synthesis-dependent first-order Raman scattering in SrTiO<sub>3</sub> nanocubes at room temperature. *Chem. Mater.* **2008**, *20*, 5628–5635.

(36) Hu, L. H.; Wang, C. D.; Kennedy, R. M.; Marks, L. D.; Poepplmeier, K. R. The Role of Oleic Acid: From Synthesis to Assembly of Perovskite Nanocuboid Two-Dimensional Arrays. *Inorg. Chem.* **2015**, *54*, 740–745.

(37) Hu, L. H.; Wang, C. D.; Lee, S.; Winans, R. E.; Marks, L. D.; Poepplmeier, K. R. SrTiO<sub>3</sub> Nanocuboids from a Lamellar Microemulsion. *Chem. Mater.* **2013**, *25*, 378–384.

(38) Setthapun, W.; Williams, W. D.; Kim, S. M.; Feng, H.; Elam, J. W.; Rabuffetti, F. A.; Poepplmeier, K. R.; Stair, P. C.; Stach, E. A.; Ribeiro, F. H.; Miller, J. T.; Marshall, C. L. Genesis and Evolution of Surface Species during Pt Atomic Layer Deposition on Oxide Supports Characterized by in Situ XAFS Analysis and Water-Gas Shift Reaction. *J. Phys. Chem. C* **2010**, *114*, 9758–9771.

(39) Crosby, L. A.; Kennedy, R. M.; Chen, B. R.; Wen, J. G.; Poepplmeier, K. R.; Bedzyk, M. J.; Marks, L. D. Complex surface structure of (110) terminated strontium titanate nanododecahedra. *Nanoscale* **2016**, *8*, 16606–16611.

(40) Christensen, S. T.; Elam, J. W.; Rabuffetti, F. A.; Ma, Q.; Weigand, S. J.; Lee, B.; Seifert, S.; Stair, P. C.; Poepplmeier, K. R.; Hersam, M. C.; Bedzyk, M. J. Controlled Growth of Platinum Nanoparticles on Strontium Titanate Nanocubes by Atomic Layer Deposition. *Small* **2009**, *5*, 750–757.

(41) Wang, C.; Hu, L.; Poepplmeier, K. R.; Stair, P. C.; Marks, L. D. Nucleation and growth process of atomic layer deposition platinum nanoparticles on strontium titanate nanocuboids. *Nanotechnology* **2017**, *28*, 185704.

(42) Chen, B. R.; George, C.; Lin, Y. Y.; Hu, L. H.; Crosby, L.; Hu, X. Y.; Stair, P. C.; Marks, L. D.; Poepplmeier, K. R.; Van Duyne, R. P.; Bedzyk, M. J. Morphology and oxidation state of ALD-grown Pd nanoparticles on TiO<sub>2</sub>- and SrO-terminated SrTiO<sub>3</sub> nanocuboids. *Surf. Sci.* **2016**, *648*, 291–298.

- (43) Lin, Y. Y.; Wen, J. G.; Hu, L. H.; Kennedy, R. M.; Stair, P. C.; Poeppelmeier, K. R.; Marks, L. D. Synthesis-Dependent Atomic Surface Structures of Oxide Nanoparticles. *Phys. Rev. Lett.* **2013**, *111*, 156101.
- (44) Enterkin, J. A.; Kennedy, R. M.; Lu, J. L.; Elam, J. W.; Cook, R. E.; Marks, L. D.; Stair, P. C.; Marshall, C. L.; Poeppelmeier, K. R. Epitaxial Stabilization of Face Selective Catalysts. *Top. Catal.* **2013**, *56* (18–20), 1829–1834.
- (45) Winterbottom, W. L. Equilibrium Shape of a Small Particle in Contact with a Foreign Substrate. *Acta Metall.* **1967**, *15* (2), 303–310.
- (46) Kang, Y.; Li, M.; Cai, Y.; Cargnello, M.; Diaz, R. E.; Gordon, T. R.; Wieder, N. L.; Adzic, R. R.; Gorte, R. J.; Stach, E. A.; Murray, C. B. Heterogeneous Catalysts Need Not Be so "Heterogeneous": Monodisperse Pt Nanocrystals by Combining Shape-Controlled Synthesis and Purification by Colloidal Recrystallization. *J. Am. Chem. Soc.* **2013**, *135*, 2741–2747.
- (47) Liu, X. J.; Wang, R.; Song, L. Y.; He, H.; Zhang, G. Z.; Zi, X. H.; Qiu, W. G. The oxidation of carbon monoxide over the palladium nanocube catalysts: Effect of the basic-property of the support. *Catal. Commun.* **2014**, *46*, 213–218.
- (48) Ino, S. Epitaxial Growth of Metals on Rocksalt Faces Cleaved in Vacuum 0.2. Orientation and Structure of Gold Particles Formed in Ultrahigh Vacuum. *J. Phys. Soc. Jpn.* **1966**, *21*, 346–362.
- (49) Ino, S.; Ogawa, S. Multiply twinned particles at earlier stages of gold film formation on alkali halide crystals. *J. Phys. Soc. Jpn.* **1967**, *22*, 1365–1374.
- (50) Allpress, J. G.; Sanders, J. V. Structure and Orientation of Crystals in Deposits of Metals on Mica. *Surf. Sci.* **1967**, *7*, 1–25.
- (51) Marks, L. D. Experimental Studies of Small-Particle Structures. *Rep. Prog. Phys.* **1994**, *57*, 603–649.
- (52) Hofmeister, H. Fivefold Twinned Nanoparticles. *Encyclopedia of Nanoscience and Nanotechnology*; American Scientific Publishers, 2004; Vol. 3, pp 431–452.
- (53) Marks, L. D.; Peng, L. Nanoparticle shape, thermodynamics and kinetics. *J. Phys.: Condens. Matter* **2016**, *28*, 053001.
- (54) Schneider, C. A.; Rasband, W. S.; Eliceiri, K. W. NIH Image to ImageJ: 25 years of image analysis. *Nat. Methods* **2012**, *9*, 671–675.
- (55) Ravel, B.; Newville, M. ATHENA, ARTEMIS, HEPHAESTUS: data analysis for X-ray absorption spectroscopy using IFEFFIT. *J. Synchrotron Radiat.* **2005**, *12*, 537–541.
- (56) Gérard Bergeret, P. G. *Handbook of Heterogeneous Catalysis*; Wiley-VCH Verlag GmbH & Co. KGaA, 2008.
- (57) Venables, J. A. Atomic Processes in Crystal-Growth. *Surf. Sci.* **1994**, *299*, 798–817.
- (58) Venables, J. A. *Growth and Properties of Ultrathin Epitaxial Layers*; King, D. A. W., Ed.; Elsevier Science, 1997; pp 1–45.
- (59) Wang, C. D.; Koirala, P.; Stair, P.; Marks, L. ALD synthesis of platinum nanoparticles on single-crystal SrTiO<sub>3</sub> pretreated with wet chemical etching. *Appl. Surf. Sci.* **2017**, *422*, 661–665.
- (60) Wang, C. D.; Hu, L. H.; Lin, Y. Y.; Poeppelmeier, K.; Stair, P.; Marks, L. Controllable ALD synthesis of platinum nanoparticles by tuning different synthesis parameters. *J. Phys. D: Appl. Phys.* **2017**, *50*, 415301.
- (61) Crosby, L. A.; Chen, B. R.; Kennedy, R. M.; Wen, J. G.; Poeppelmeier, K. R.; Bedzyk, M. J.; Marks, L. D. All Roads Lead to TiO<sub>2</sub>: TiO<sub>2</sub>-Rich Surfaces of Barium and Strontium Titanate Prepared by Hydrothermal Synthesis. *Chem. Mater.* **2018**, *30*, 841–846.
- (62) Kienzle, D. M.; Becerra-Toledo, A. E.; Marks, L. D. Vacant-Site Octahedral Tilings on SrTiO<sub>3</sub> (001), the (root 13 x root 13)R33.7 degrees Surface, and Related Structures. *Phys. Rev. Lett.* **2011**, *106*, 176102.
- (63) Enterkin, J. A.; Subramanian, A. K.; Russell, B. C.; Castell, M. R.; Poeppelmeier, K. R.; Marks, L. D. A homologous series of structures on the surface of SrTiO<sub>3</sub>(110). *Nat. Mater.* **2010**, *9* (3), 245–248.
- (64) Ino, S. Stability of Multiply-Twinned Particles. *J. Phys. Soc. Jpn.* **1969**, *27*, 941–953.
- (65) Avery, N. R.; Sanders, J. V. Structure of Metallic Particles in Dispersed Catalysts. *J. Catal.* **1970**, *18*, 129.
- (66) Marks, L. D.; Howie, A. Multiply-Twinned Particles in Silver Catalysts. *Nature* **1979**, *282*, 196–198.
- (67) Lear, T.; Marshall, R.; Lopez-Sanchez, J. A.; Jackson, S. D.; Klapotke, T. M.; Baumer, M.; Rupprechter, G.; Freund, H. J.; Lennon, D. The application of infrared spectroscopy to probe the surface morphology of alumina-supported palladium catalysts. *J. Chem. Phys.* **2005**, *123*, 174706.
- (68) Santra, A. K.; Goodman, D. W. Catalytic oxidation of CO by platinum group metals: from ultrahigh vacuum to elevated pressures. *Electrochim. Acta* **2002**, *47*, 3595–3609.
- (69) Wolter, K.; Seiferth, O.; Kuhlenbeck, H.; Baumer, M.; Freund, H. J. Infrared spectroscopic investigation of CO adsorbed on Pd aggregates deposited on an alumina model support. *Surf. Sci.* **1998**, *399*, 190–198.
- (70) Bensalem, A.; Muller, J. C.; Tessier, D.; Bozon-Verduraz, F. Spectroscopic study of CO adsorption on palladium-ceria catalysts. *J. Chem. Soc., Faraday Trans.* **1996**, *92*, 3233–3237.
- (71) Sa, J.; Arteaga, G. D.; Daley, R. A.; Bernardi, J.; Anderson, J. A. Factors influencing hydride formation in a Pd/TiO<sub>2</sub> catalyst. *J. Phys. Chem. B* **2006**, *110*, 17090–17095.
- (72) Ertl, G.; Norton, P. R.; Rustig, J. Kinetic Oscillations in the Platinum-Catalyzed Oxidation of Co. *Phys. Rev. Lett.* **1982**, *49*, 177–180.
- (73) Engel, T.; Ertl, G. Elementary Steps in the Catalytic Oxidation of Carbon Monoxide on Platinum Metals. *Adv. Catal.* **1979**, *28*, 1.
- (74) Berlowitz, P. J.; Peden, C. H. F.; Goodman, D. W. Kinetics of Co Oxidation on Single-Crystal Pd, Pt, and Ir. *J. Phys. Chem.* **1988**, *92*, 5213–5221.
- (75) Kunz, S.; Schweinberger, F. F.; Habibpour, V.; Rottgen, M.; Harding, C.; Arenz, M.; Heiz, U. Temperature Dependent CO Oxidation Mechanisms on Size-Selected Clusters. *J. Phys. Chem. C* **2010**, *114*, 1651–1654.
- (76) Engel, T.; Ertl, G. A molecular beam investigation of the catalytic oxidation of CO on Pd (111). *J. Chem. Phys.* **1978**, *69*, 1267–1281.
- (77) Meusel, I.; Hoffmann, J.; Hartmann, J.; Heemeier, M.; Baumer, M.; Libuda, J.; Freund, H. J. The interaction of oxygen with alumina-supported palladium particles. *Catal. Lett.* **2001**, *71*, 5–13.
- (78) Peter, M.; Adamovsky, S.; Flores Camacho, J. M.; Schauerermann, S. Energetics of elementary reaction steps relevant for CO oxidation: CO and O<sub>2</sub> adsorption on model Pd nanoparticles and Pd(111). *Faraday Discuss.* **2013**, *162*, 341–354.
- (79) Cassidy, T. J.; Allen, M. D.; Li, Y.; Bowker, M. From Surface Science to Catalysis - Surface Explosions Observed on Rh Crystals and Supported Catalysts. *Catal. Lett.* **1993**, *21*, 321–331.
- (80) Mhatre, B. S.; Pushkarev, V.; Holsclaw, B.; Lawton, T. J.; Sykes, E. C. H.; Gellman, A. J. A Window on Surface Explosions: Tartaric Acid on Cu(110). *J. Phys. Chem. C* **2013**, *117*, 7577–7588.